


Comparisons of Dynamic Landslide Models on GIS Platforms

Yuming Wu ¹, Aohua Tian ^{1,2,3} and Hengxing Lan ^{1,*}

¹ State Key Laboratory of Resources and Environmental Information System, Institute of Geographic Sciences and Natural Resources Research, Chinese Academy of Sciences, Beijing 100101, China; wuym@reis.ac.cn (Y.W.); tian1454565116@163.com (A.T.)

² College of Geoscience and Surveying Engineering, China University of Mining and Technology-Beijing, Beijing 100083, China

³ College of Resources and Environment, University of Chinese Academy of Sciences, Beijing 100049, China

* Correspondence: lanhx@reis.ac.cn; Tel.: +86-10-64888783

Abstract: Numerical simulation is one of the methods to assess landslide movement processes, which is beneficial for engineering design and urban planning. With the development of computer technology, GIS has gradually become the mainstream platform for landslide simulation due to data availability and algorithm integrability. However, the dynamic processes of landslides are complicated, which makes integration difficult on GIS platforms. Some assumptions are applied to simplify these dynamic processes and solve this problem. Generally, there are two main types of numerical models on GIS platforms: models based on the Eulerian description and models based on the Lagrangian description. Case studies show that Eulerian models are suitable for flow-like movement, and Lagrangian models are suitable for discrete rigid bodies movement. Different models face different problems: the Eulerian-based models show numerical diffusion and oscillation, and the Lagrangian-based model needs to consider complicated shear and collision processes. In addition, the 3-D model can describe more details in the z-direction, while the depth-averaged model can obtain a reasonable range of motion, depth, and speed quickly. From the view of numerical simulation, inappropriate models, assumptions, and numerical schemes will produce errors. The landslide type refers to several forms of mass wasting associated with a wide range of ground movements, which guides establishing dynamic models and numerical schemes on GIS platforms and helps us obtain results accurately.

Keywords: landslide dynamics; landslide classification; dynamic models; depth-averaged model; GIS



Citation: Wu, Y.; Tian, A.; Lan, H. Comparisons of Dynamic Landslide Models on GIS Platforms. *Appl. Sci.* **2022**, *12*, 3093. <https://doi.org/10.3390/app12063093>

Academic Editors: Ricardo Castedo, Miguel Llorente Isidro and David Moncoulon

Received: 18 February 2022

Accepted: 16 March 2022

Published: 17 March 2022

Publisher's Note: MDPI stays neutral with regard to jurisdictional claims in published maps and institutional affiliations.



Copyright: © 2022 by the authors. Licensee MDPI, Basel, Switzerland. This article is an open access article distributed under the terms and conditions of the Creative Commons Attribution (CC BY) license (<https://creativecommons.org/licenses/by/4.0/>).

1. Introduction

Landslides cause a large number of casualties and property losses every year. Quantitative risk analysis (QRA) is essential for reducing property damage and loss of life. Numerical simulation is one of the methods for assessing the landslide movement process and potential hazard levels [1,2], which is part of quantitative risk analysis [3]. Many numerical models are used to obtain the landslide runout distance, thus providing a basis for urban planning [4–7].

From dynamics, all landslides follow Newton's second law [2] and, thus, mass conservation, momentum conservation, and energy conservation are the governing equations in numerical simulations. In terms of force, gravity is the primary driving force [8], and friction is the major resistance force during motion. However, different shear processes and collision processes make landslide dynamics complex.

There are two model types: discrete models and continuum models. The discrete models describe the interactions and shocks well, but the continuum models describe the flow well. The Lagrangian functions describe the translation and rotation of each discrete element for the discrete models. Eulerian functions are the best to calculate the field for the continuum models. With the development of computation, meshless methods such as

SPH are proposed to solve problems dominated by complex boundary dynamics for the continuum models. In the SPH method, finding neighboring nodes is difficult. Models with different accuracies are used to describe the processes [7]. These models include Rockfall Analyst [9], Rocfall [10], and Rockyfor3D [11] for rockfalls, and Massflow [12], Flo-2D [13], r.avaflow [14], and Titan2D [15] for mass flow.

In some simulations, different software programs yield different trajectories based on methods, assumptions, and numerical schemes [16]. Models may face various challenges. For example, fluid mechanics models may encounter numerical diffusions and oscillations [17]; rigid body models need to consider complicated shear and collision processes [18]. Therefore, a suitable model is a prerequisite for obtaining accurate results, and the physical insights provided by models can help us understand the landslide process.

GIS provides some functions that allow users to build numerical models [19]. It makes programming convenient and easy. There are two types of landslide simulations on GIS platforms: add-in programs and stand-alone programs. Add-in programs use the GUI and functions on GIS platforms to build a dynamic landslide model. This combination is easy to implement, but the GIS platform may limit some capacities. Stand-alone programs use open libraries such as GDAL. They are computationally efficient but require a lot of development time. The landslide dynamics programs on GIS platforms need to be simplified to accommodate the GIS file structure. Therefore, appropriate assumptions and suitable models are the keys to simulation on GIS platforms.

Landslide classification uses simple words to describe the characteristics of landslide phenomena, which may guide us to select a suitable model for simulation on GIS platforms. Several authors, including Heim [20], Zaruba and Mencl [21], and Sharpe [22], proposed different landslide classification systems. In most of these classifications, the name of the landslide is a combination of the material and motion type [23–26]. The most well-known classification system is Varnes' classification [27]. In this classification, material types include rock, debris, and earth, and motion types include falling, toppling, sliding, spreading flow, and complex. Subsequently, Hungr [23] updated the Varnes' classification to assess landslide phenomena, and the material types were more detailed than those in the original classification. Landslide types are often indicators of the critical movement process, and a suitable numerical model must consider the appropriate variables.

However, the relationship between the landslide movement process and the physical mechanism of landslides is not very clear. It results in difficulty in obtaining accurate runout zones on GIS platforms. In this paper, we compared numerical models on GIS platforms and established relationships between landslide types and the selection of numerical models on GIS platforms.

2. Models

2.1. Descriptions

Landslides contain two main motion processes: rigid body motion and flow-like motion. The rigid body motion assumes that the block does not deform or change shape [28]; the flow-like motion assumes that the material is continuous mass rather than discrete particles. The driving force is gravity, and the resistance force is mainly friction during the movement (Figure 1).

In dynamics, there are five major categories in the Varnes' movement type: falling, toppling, sliding, spreading, and flowing. The movement type is related to the critical processes that occur during motion. All the processes follow Newton's laws of motion [29,30], which are given by

$$\frac{dmv}{dt} = f \quad (1)$$

where m is the mass, v is the velocity, and f is the resultant force, which depends on the movement type. The left-hand side (LHS) of Equation (1) represents the motion process, and the right-hand side (RHS) is the resultant force.

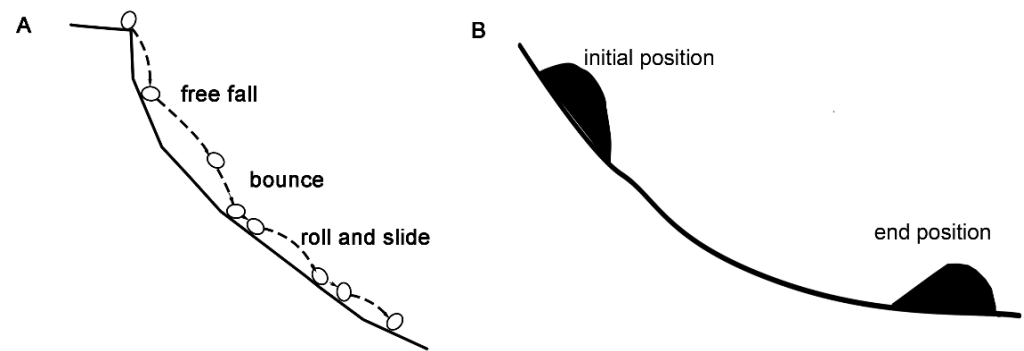
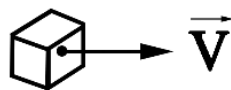


Figure 1. Two main motion processes: (A) the rigid body motion, and (B) the flow-like motion.

There are two common descriptions of motion in numerical models: the Eulerian description and the Lagrangian description [31] (Figure 2). In the Eulerian description, a model is not concerned about the location or velocity of any particular particle or columns, and the focus is on the grid. In the Lagrangian description, individual particles or columns are marked, and their positions and velocities are described as a function of time.

Eulerian

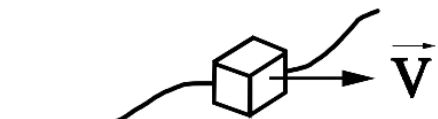
Fixed cell



$h(x,y,z,t)$

Lagrangian

moving with object



$h(t)$

Figure 2. Eulerian and Lagrangian descriptions.

2.1.1. Models Based on the Lagrangian Description

The rigid body motion includes translation and rotation, which are six-degrees-of-freedom processes (three components for the translation process and three components for the rotation process). Using the center of mass and inertia matrix, the force and torque equations take the form:

$$\mathbf{F} = m\mathbf{a}, \mathbf{T} = [I_R]\alpha + \omega \times [I_R]\omega \tag{2}$$

where \mathbf{F} is the force, \mathbf{T} is the torque, \mathbf{a} is the acceleration, m is the mass, I_R is the moment of inertia matrix, ω is the angular velocity, and α is the angular acceleration. The equations of translation and rotation on the Lagrangian description are

$$\mathbf{x}_{t+\Delta t} = \mathbf{x}_t + \mathbf{v}_t\Delta t + \frac{1}{2}\mathbf{a}_t\Delta t^2 \tag{3}$$

$$\theta_{t+\Delta t} = \theta_t + \omega_t\Delta t + \frac{1}{2}\alpha_t\Delta t^2 \tag{4}$$

where \mathbf{x}_t is the location at time t , \mathbf{v}_t is the velocity at time t , \mathbf{a}_t is the acceleration at t , θ_t is the angle at time t , ω_t is the angular velocity at time t , and α_t is the angular acceleration at time t .

2.1.2. Models Based on the Eulerian Description

In the continuum systems, the Eulerian description is best for simulating motion, and the Navier–Stokes equations are the basis of modeling [32]:

$$\frac{\partial \rho}{\partial t} + \nabla \cdot (\rho \mathbf{v}) = 0 \tag{5}$$

$$\rho(\partial \mathbf{v} / \partial t + \mathbf{v} \cdot \nabla \mathbf{v}) = \mathbf{S}_f \tag{6}$$

where ρ is the mass density, t is time, \mathbf{v} is the velocity, \mathbf{S}_f is the field which includes gravity, friction, and other forces. The best way to solve these equations is through numerical analysis due to lacking a smooth analytical solution. Traditional CFDs such as Openfoam® use these equations to simulate the landslide dynamics. In these programs, the geometric modeling process is complex.

To describe flowing grain–fluid mixture, Iverson proposed a mixture theory [33], and the \mathbf{S}_f is:

$$\mathbf{S}_f = -\nabla \cdot (\mathbf{T}_s + \mathbf{T}_f + \mathbf{T}') + \rho \mathbf{g} \tag{7}$$

in which

$$\rho = \rho_s v_s + \rho_v v_v \tag{8}$$

$$\mathbf{v} = (\rho_s v_s \mathbf{v}_s + \rho_f v_f \mathbf{v}_f) / \rho. \tag{9}$$

Here, ρ is the mixture mass density, \mathbf{v} is the mixture velocity, \mathbf{v}_s is the velocity in the solid phase and \mathbf{v}_f is the velocity in the fluid phase, v_s is the volume fraction of solid, v_f is the volume fraction of fluid, \mathbf{g} is the gravitational acceleration, \mathbf{T}_s is the solid stress, \mathbf{T}_f is the fluid stress, and \mathbf{T}' is a contribution to the mixture stress. The stress \mathbf{T}' can be avoided by using an approximation suitable for many debris flows.

To reduce the difficulty of traditional CFDs, Savage and Hutter proposed the depth-averaged theory [34]. This model allows the GIS to integrate simulation codes. Depth averaging is one of the steps to eliminate the calculation in the z -direction. The averaged velocities and resultant forces are calculated on the x – y plane [32,34,35]. In this method, the assumption is that ρ is constant and the landslide depth is shallow. Thus, the equations [32,36] are

$$\frac{\partial h}{\partial t} + \frac{\partial h \bar{v}_x}{\partial x} + \frac{\partial h \bar{v}_y}{\partial y} = 0 \tag{10}$$

$$\rho \left[\frac{\partial (h \bar{v}_x)}{\partial t} + \frac{\partial (h \bar{v}_x^2)}{\partial x} + \frac{\partial (h \bar{v}_x \bar{v}_y)}{\partial y} \right] = - \int_0^h \left[\frac{\partial T_{xx}}{\partial x} + \frac{\partial T_{yx}}{\partial y} + \frac{\partial T_{zx}}{\partial z} - \rho g_x \right] dz \tag{11}$$

$$\rho \left[\frac{\partial (h \bar{v}_y)}{\partial t} + \frac{\partial (h \bar{v}_y^2)}{\partial y} + \frac{\partial (h \bar{v}_x \bar{v}_y)}{\partial x} \right] = - \int_0^h \left[\frac{\partial T_{xy}}{\partial x} + \frac{\partial T_{yy}}{\partial y} + \frac{\partial T_{zy}}{\partial z} - \rho g_y \right] dz. \tag{12}$$

where $\bar{v}_x = \frac{1}{h} \int_0^h v_x dz$, $\bar{v}_y = \frac{1}{h} \int_0^h v_y dz$. As shown in the equations, the velocity in the z -direction is averaged. Based on the depth-averaged theory, a depth-averaged mixture model was proposed by Iverson and Denlinger [32]. Subsequently, two-phase and multi-phase depth-averaged models were proposed to describe distinct mechanical responses and dynamic behaviors of material [35,37].

Some studies considered the erosion process, a mechanical process by which the bed material is mobilized by the flow and dominant mechanical processes in geophysical mass flows [38]. Erosion determines enhanced or reduced mobility but is not understood thoroughly. In the dynamic model, the erosion rate $E = -\partial b / \partial t$ and erosion velocity u_b are two important parameters, which change mass and momentum productions E and $u_b E$ [38], respectively. Subsequently, Pudashini and Fischer proposed a two-phase erosion model on this basis [39]. The emergence of these models has further developed the continuum model on GIS platforms.

2.2. Forces

Gravity, friction, collision force, and hydraulic pressure are the major forces during motion. Some forces have less influence and can be ignored during the movement.

2.2.1. Collision Force

Collision force is one of the factors affecting the process of landslide movement, especially during falls and topples. The collision process is complicated, which makes the calculation difficult. Traditionally, the spring–dashpot model is widely used to describe the nonlinear process, which is

$$F_n = F_{el} + F_{diss} \quad (13)$$

where F_n is the collision force, F_{el} is the elastic force (spring), and F_{diss} is the dissipative force (dashpot). The spring obeys Hooke's law, and the dashpot obeys Newton's law of viscosity [40,41]. To simplify the process, Evans and Hungr used a lumped mass model in ROCKFALL programs in 1993 [42]. The associated assumptions of the lumped mass model are as follows: (1) each rock is a small spherical particle; (2) rocks do not have any size, only mass. The lumped mass model uses one or two restitution coefficients to express this process to avoid calculating complex collision forces. The restitution coefficients are the ratio of the rebound velocity to the incident velocity, the impulse ratio, and the work ratio, which involves the square root of work performed. Most models use two restitution coefficients: the tangential restitution coefficient R_t and the normal restitution coefficient R_n ; however, a few models use only one restitution coefficient to quantify dissipation in terms of velocity magnitude loss. Hybrid approaches were proposed on GIS platforms to simulate rockfall accurately. These models, such as CRSP [43], RocFall [44], and STONE [45], consider the influence of shape and nonlinear collision based on the lumped mass model. Hybrid approaches have been the mainstream models on GIS platforms. Therefore, there are three models for describing the collision force, a fully rigid body model, a lumped mass model, and a hybrid approach [46], on GIS platforms.

2.2.2. Friction Force

Friction is the force that resists the relative motion of solid surfaces, fluid layers, and material elements sliding against each other, which is important for the movement calculation. In this process, kinetic energy is converted to thermal energy when motion with friction occurs. There are two types of resistance: viscosity and Coulomb's friction.

For dry granular flow, Coulomb's friction is adopted, which is

$$\tau = \mu N \quad (14)$$

where τ is the unit base resistance and μ is the friction coefficient, and N is the normal force. Generally, the basal shear forces, obtained by simple infinite landslide models, are calculated by Coulomb's friction.

For fluid flow, viscosity is a measure of resistance to deformation at a given rate. It can be conceptualized as the internal frictional force that arises between adjacent layers of fluid that are in relative motion. There are three viscosity equations: Newtonian, Bingham, and quadratic fluids.

(1) The Newtonian fluid is:

$$\tau = \mu \gamma' \quad (15)$$

where μ is the shear viscosity of a fluid and γ' is the derivative of the velocity component.

(2) The Bingham fluid model is

$$\tau = \tau_0 + \mu \gamma' \quad (16)$$

where τ_0 is a constant yield strength, μ is the shear viscosity of the fluid, and γ' is the derivative of the velocity component.

(3) The quadratic fluid model is

$$\tau = \tau_0 + \mu\gamma' + \zeta\gamma'^2 \tag{17}$$

The first two terms are referred to as the Bingham shear stresses. The last term represents the dispersive and turbulent shear stresses. Fluid friction can be generalized as:

$$f = f_s + f_v + f_t \tag{18}$$

where f_v is the viscosity term, f_s is the constant term, and f_t is a turbulent term. Based on the depth-averaged theory, shear stress is depth-integrated, and the corresponding equation is

$$S = \frac{1}{h} \int f dz \tag{19}$$

where S is depth-integrated shear stress. Therefore, Equation (18) can be transformed to:

$$S_{fx} = S_\tau + S_v + S_{td}. \tag{20}$$

2.2.3. Other Forces

Hydraulic pressure in the depth-averaged model is the force imparted per unit area of liquid or flow-like materials on the surfaces, which can be expressed in the Eulerian description as:

$$F_i = \frac{\partial}{\partial x} \beta \frac{h^2}{2} \tag{21}$$

where β can be changed to β_s^x and β_f^x based on the form of the phase [37]. For fluid, the β is g^z . For solids, the force created by collisions among particles is simplified to an internal force based on soil mechanics, and the β is:

$$\beta_s^x = Kg^z(1 - \gamma_s^f) \tag{22}$$

$$K_{pas/act} = 2 \sec^2 \phi \left\{ 1 \pm (1 - \cos^2 \phi \sec^2 \delta)^{1/2} \right\} - 1 \tag{23}$$

where ϕ is the internal frictional angle and δ is the basal frictional angle. The collisions and frictions among particles are difficult to calculate during the motion.

There are two methods to describe the form of hydraulic pressure on the Lagrangian description. The first method is the particle-in-cell (PIC) method [47], which converts particles or columns to fields based on the volume in each cell. The other is smoothed-particle hydrodynamics (SPH) approximation [48–50], and they are:

$$\bar{P}_I = \frac{1}{2} \beta h_I^2 \tag{24}$$

$$H_p = \sum_J m_J \left(\frac{\bar{P}_I}{h_I^2} + \frac{\bar{P}_J}{h_J^2} \right) grad W_{IJ} \tag{25}$$

where \bar{P}_I is an averaged hydraulic pressure term, W_{IJ} is the value of the SPH kernel function W_{IJ} centered at node I evaluated at node J . The weighting function or kernel W_{IJ} is a symmetric function of $x_I - x_J$. Additionally, m_J has no physical meaning. When the node moves, the material contained in a column of base Ω_I has entered it or will leave it as the column moves with an averaged velocity, which is not the same for all particles or columns in it [48].

In addition, buoyancy and drag forces in the two-phase and multi-phase flow can also influence the landslide motion. Buoyancy is an upward force exerted by a fluid that opposes

the weight of a partially or fully immersed object, and it is a vertical force. Buoyancy can reduce the pressure at the basal surface. Therefore, buoyancy can reduce the resistance, especially in multi-phase flow. Drag forces are shear forces caused by different velocities and accelerations in different phases. In other words, solid particles may accelerate relative to fine solids or fluids [37].

3. Software

With the development of computer technology, GIS has gradually become a mainstream system for engineering design and urban planning. There are a lot of GIS programs, such as GRASS GIS, QGIS, and ArcGIS. GRASS GIS and QGIS are popular in program development due to being free and open source. ArcGIS is a mature commercial program and is widely applied in urban planning and engineering design. These programs provide a rich interface such as raster import, vector import, raster statistics, and vector analysis, and are convenient for users to call the functions and develop their programs. In addition, these programs provide a GUI to display the results calculated by their programs. More and more landslide simulation codes support GIS. At present, there are two kinds of programs: programs based on the rigid body model and programs based on the flow-like model.

3.1. Programs Based on the Rigid Body Model

On GIS platforms, there are several programs to simulate the discrete rigid body motions, as shown in Table 1. On GIS platforms, the format of input parameters of GIS data needs to be considered, especially DEM data. The choice of parameter expressions determines the model. There are three types of DEMs to express on GIS platforms: triangulated irregular networks (TINs), grid networks, and vector or contour-based networks. Relying on the algorithm, the selection of the DEM is also different. For example, Rockfall Analyst and Rockyfor3D select the grid networks. The lumped mass models are popular in early GIS platforms among these models. With the GIS technique development, the hybrid model is mainstream on GIS platforms. These programs include Hy-STONE, Rockyfor3D, and PICUS Rock’n’Roll.

Table 1. Rigid body programs on GIS platforms.

Software	Scheme	Platform	Format
STONE [45]	Lumped mass		ASCII
Hy-STONE [51]	Hybrid		ASCII
Rockfall Analyst [9]	Lumped mass	ArcGIS	All raster format
Rockyfor3D [11]	Hybrid		ASCII
PICUS Rock’n’Roll [52]	Hybrid	PICUS	
RAMMS::ROCKFALL [53]	Rigid body		ASCII
RockGIS [54]	Lumped mass		ASCII

3.2. Programs Based on the Flow-like Model

Based on the description, the grid networks of DEM are best for flow-like models on GIS platforms. The grid networks make the calculation simple and accurate. At present, there are a lot of codes on the GIS platforms, such as r.avaflow, LA, DA, Titan2D, and Massflow (Table 2). As for the model, the depth-averaged theory model is employed to obtain the depths and velocities in each cell. The simulation r.avaflow is popular around the world. The program has a built-in multi-phase flow method based on the depth-averaged theory and is applied in GRASS GIS and R. It is a very good cross-platform program, which means that we can use the program on Windows, Linux, and Mac OS [35,37,38].

Table 2. Flow-like programs on GIS platforms.

Software	Description	Scheme	Format	Platform
r.avaflow [14]	Eulerian	NOC	All raster format	GRASS
RAMMS [55]	Eulerian	1st/2nd order	ASCII, Geotiff	
Massflow [12]	Eulerian	TVD–MacCormack	ASCII	
Massmov2D [56]	Eulerian	2-step scheme	PCRaster	PCRaster
LA and DA [31,57]	Eulerian–Lagrangian	PIC-like	GeoTIFF	
Titan2D [15]	Eulerian	AMR	All raster format	GRASS
IMEX_SfloW2D [58]	Eulerian	Semi-discrete central scheme	ASCII	
Geo-Claw [59]	Eulerian	AMR	ASCII, NetCDF	
FLO-2D [13]	Eulerian	1st order	All raster format	QGIS
DAN3D [60]	Lagrangian	SPH	ASCII	
SPHERA [61]	Lagrangian	SPH	All raster format	QGIS

For flow-like programs, the numerical scheme is one of the factors affecting results. Most codes use 1st or 2nd order finite difference methods to solve the partial differential equations. In these programs, the numerical diffusion and numerical oscillation are the difficulties for the models in the Eulerian description. Some codes use the TVD method and adaptive mesh refinement (AMR) to improve precision. In addition, some methods use the Lagrangian or Eulerian–Lagrangian description to solve difficulties such as the material point method (MPM) [62], particle-in-cell (PIC) [47], and smoothed particle hydrodynamics (SPH) [63]. In these models, the computational cost of simulations per number of particles may be higher than the cost of grid-based simulations per number of cells. In some cases, these methods solve the numerical solution problem of differential equations to a certain extent.

4. Results and Discussion

Many factors affect the simulation results, such as models, algorithms, and descriptions. In this section, we show cases such as bilateral dam break, a rockfall example in the RA program, and the Yigong landslide to analyze the effect on models, algorithms, and descriptions.

4.1. Reason for Differences

4.1.1. Differences Caused by Models

Different models can produce different results due to assumptions. We used a 2-D bilateral dam break simulation to analyze the applicability of the traditional CFD model (two-phase model), the depth-averaged model, and the SPH model (Figure 3). In these simulations, we set the initial state to 1 m at [0, 1]. Under the action of gravity, the fluid moves downward. In this case, we applied the interfoam solver of OpenFOAM[®] to calculate the two-phase model [64], PySPH to calculate the SPH model [65], and the Lax–Friedrichs scheme to calculate the depth-averaged model. In OpenFOAM[®], we select the area in the grid with water content greater than 0.6 to obtain the profile. In the SPH model, we set the ball to have a diameter of 0.03 m.

The results show that the range of movement observed in all models is similar at 0.5 s, spanning [−2, 3]. In the 2-D simulation, different models will have different results in terms of details. The depth-averaged model can obtain a smoother result than the other models. Additionally, the results of the two-phase model and the SPH model include more details in the z-directions than the depth-averaged model. Based on the above analysis, the model selection depends on the relevant requirements. When detailed information is required, we must select a complex model to calculate the results. When we focus on the range, we can use the depth-averaged model.

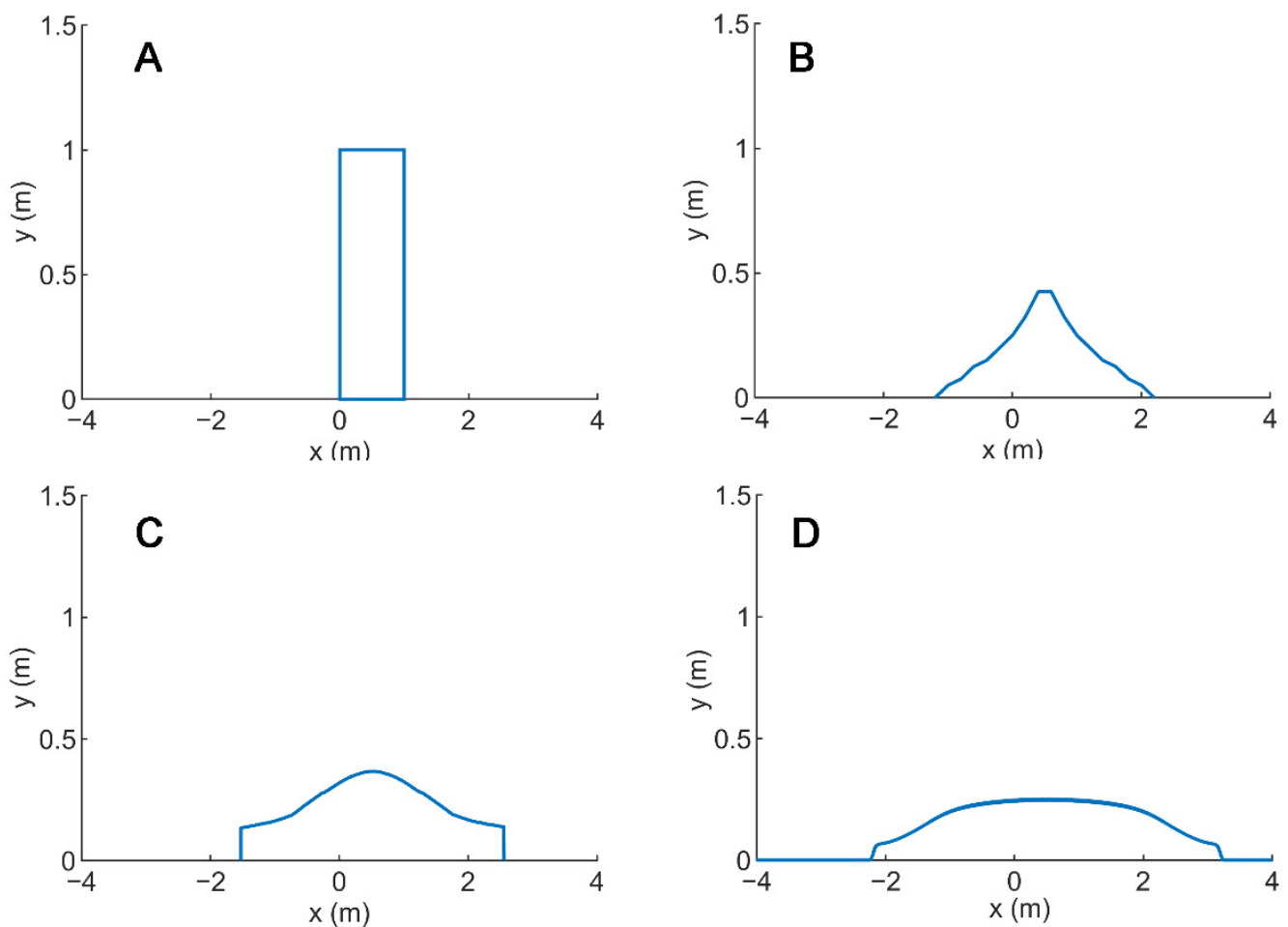


Figure 3. Bilateral dam break simulation with different models: (A) the initial state of the simulation, (B) obtained by OpenFOAM at 0.5 s, (C) obtained by PySPH at 0.5 s, and (D) obtained by the depth-averaged model at 0.5 s.

4.1.2. Differences Caused by Algorithms

Differences in parameters and numerical schemes can affect the runout zones significantly (Figure 4). In this case, we used Rockfall Analyst to analyze the influence of algorithms. The results obtained with ArcGIS 9.x and ArcGIS 10.x differ because of different point extraction algorithms (Figure 4). The small difference in the point extraction of the GIS module will affect the runout zone. The rock fell into the river in ArcGIS 9.x. However, the rock stops on the road in ArcGIS 10.x, although the DEM is the same. The results show that a small difference in the algorithm can produce large differences in trajectory.

In the Eulerian-based model, some numerical schemes can handle one property of ADEs but process badly with another one [17]. Therefore, the balance between numerical diffusion and numerical oscillation is key to obtaining a suitable physical solution. For the model in the Eulerian description, we simulated the uniform linear motion of a block with 1 m/s. In this simulation, the space interval is 0.1 m, and the time interval is 0.01 s. The Lax–Friedrichs scheme, a first-order in time and second-order in space method, shows numerical diffusion during motion (Figure 5A) but the Lax–Wendroff scheme, a second-order in both space and time method, shows numerical dispersion (Figure 5B). The errors are generally caused by neglecting high-order terms. However, higher-order linear schemes such as 3rd order, although more accurate for smooth solutions, are not TVD and tend to introduce spurious oscillations (wiggles) where discontinuities or shocks arise. Various high-resolution schemes use flux/slope limiters to maintain the TVD, thereby reducing the impact of numerical dissipation and numerical diffusion [66,67]. In these methods, the

accuracy is high in the smooth area, and the flux/slope limiter method is used in the shock area to avoid producing nonphysical solutions.

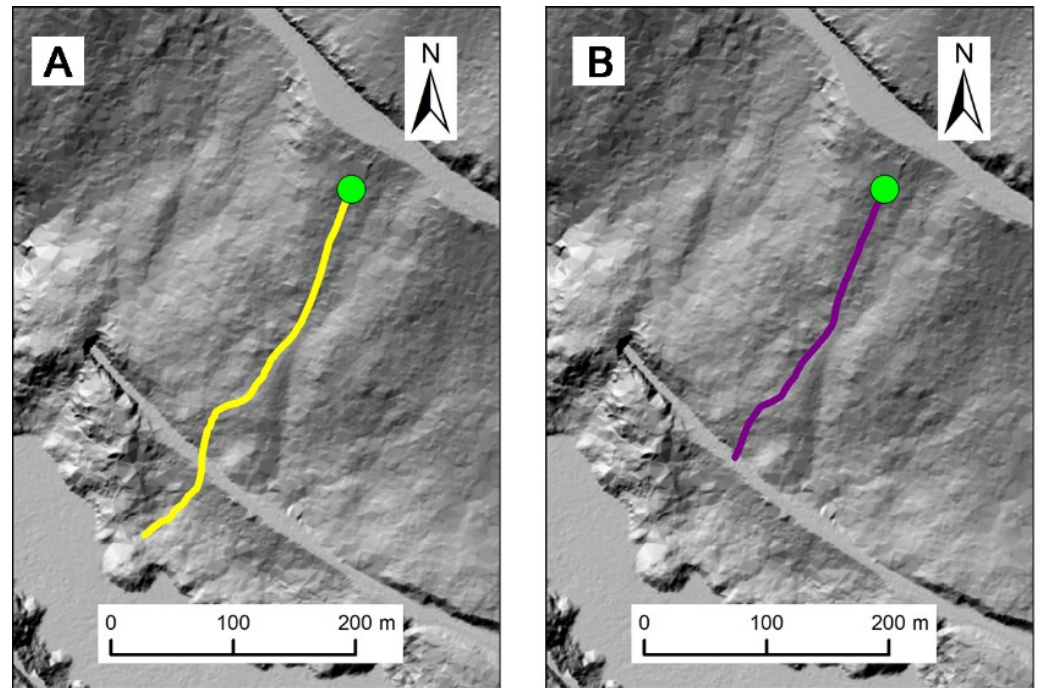


Figure 4. Rockfall simulations using RA: (A) in ArcGIS 9.x and (B) in ArcGIS 10.x.

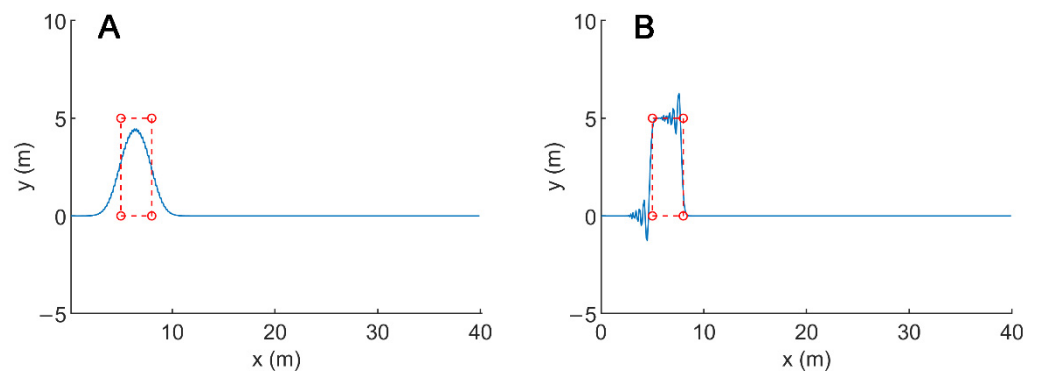


Figure 5. Numerical diffusion and numerical oscillation: (A) numerical diffusion obtained by the Lax–Friedrichs scheme, and (B) numerical oscillation obtained by the Lax–Wendroff scheme.

4.1.3. Differences Caused by Description

In this section, we show the 3-D sliding block used to analyze the influence of different descriptions. In this case, we assumed the acceleration in the x - and y -direction is 5 m/s^2 , and that the x -direction and y -direction interval is 10 m. The location of the center of the block is (200, 200) (Figure 6A). In this motion process, the deformation of the block is zero, and the block can be considered as a rigid body. After 20 s, the block moves to (1200, 1200) based on Newton’s second law. We selected the lumped mass model in the Lagrangian description and the depth-averaged model in the Eulerian description to simulate the same motion.

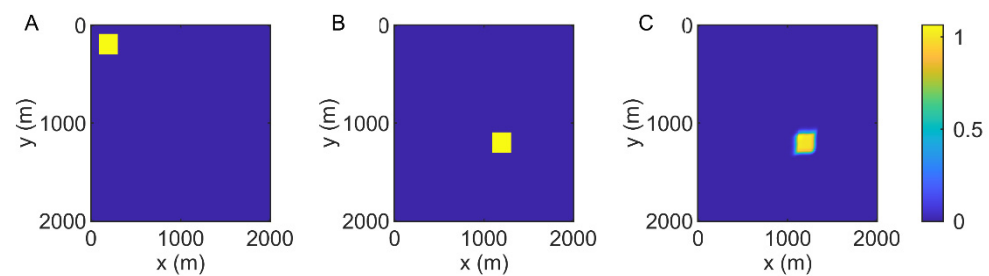


Figure 6. Simulations using different numerical schemes: (A) the original location, (B) the result in the Lagrangian description, and (C) the result in the Eulerian description.

In the Lagrangian description, the lumped mass model is simple (Figure 6B) because the block assumes a mass point in the model. Based on the lumped mass model, we can calculate the location and the result close to the observed one. In the Eulerian description, we used depth-averaged theory and the McCormack–TVD scheme. After 20 s, the block also moves to (1200, 1200) (Figure 6C). However, numerical diffusion (the green area) is notable at the boundary of the block, even though the TVD method is applied to reduce diffusion (Figure 6C). Additionally, the calculation efficiency is far lower than the method based on the Lagrangian description, when reaching the same precision. This case shows that proper model assumptions are a prerequisite for good results. Suitable assumptions can reduce some errors in the calculation process. The lumped mass model is simple and obtains results quickly and accurately. Therefore, the lumped mass model is more suitable for this motion.

In the 3-D landslide simulation, we selected the Yigong landslides to evaluate the influence of different numerical schemes. The Yigong landslide happened at the head of the Zhamulong gully (30.178° N; 94.940° E) on 9 April 2000 [68] and blocked the Yi Gong River at the foot of the slope with $3 \times 10^8 \text{ m}^3$ of sediment that formed a 60 m high dam [69]. Aiming at the characteristics of long-distance and high-speed movement of the Yigong landslide, researchers use many numerical models to investigate it.

We selected different descriptions to simulate this process. Based on previous studies [70,71], the Voellmy model can obtain a suitable result [72]. In this case, the basal friction angle is 12° , the internal friction angle is 13° , and the turbulence assumes $1000 \text{ s}^2/\text{m}$ (Table 3).

Table 3. Mechanical parameters of the Yigong landslide.

Parameters	Values
Basal friction angle	12°
Internal friction angle	13°
Turbulent coefficient	1000

In numerical schemes, we selected the NOC–TVD scheme in the Eulerian description, which is applied in r.avaflow, and the depth-averaged SPH method in the Lagrangian description to analyze the differences. The states of 50 s, 100 s, and 200 s using two methods are given in Figure 7. From the simulation, both methods obtain similar results. The Yigong landslide reached the foot of the mountain at 200 s. In detail, the process calculated in the Eulerian description is smoother than that in the Lagrangian description. The material in the Lagrangian description is concentrated in the channel. The maximum height is higher than the model in the Eulerian description. As for the maximum speed, the NOC–TVD scheme is 90.23 m/s, and the depth-averaged SPH is 97.20 m/s. The precision of the SPH model is related to the number of particles or the number of columns. The more particles or columns, the finer the description and the closer to the analytical solution of the fluid equation. Fewer particles or columns will result in lower interaction forces between columns or particles. Additionally, the computational cost of SPH simulations per number

of particles or columns is significantly larger than the cost of grid-based simulations for flow-like motion.

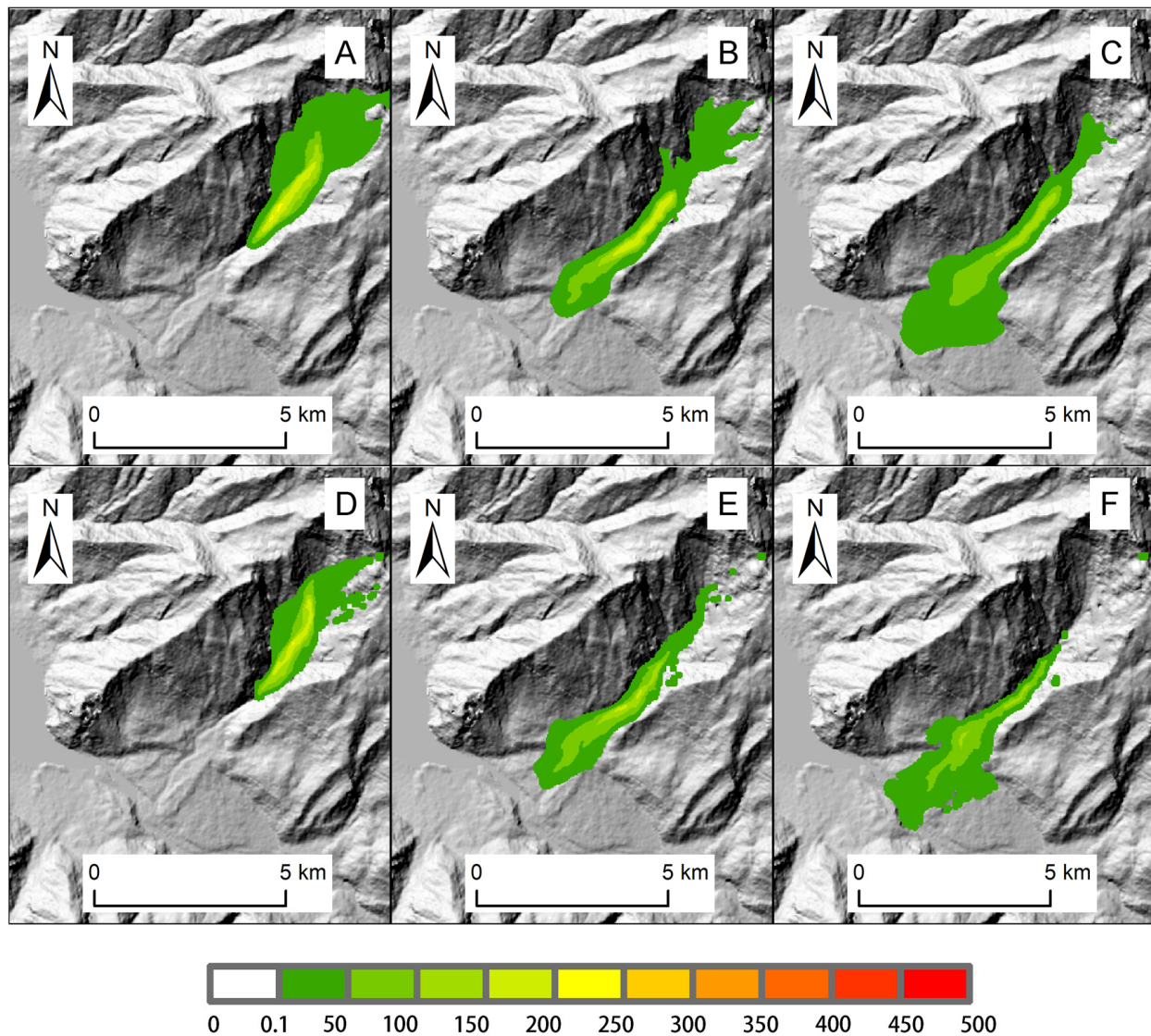


Figure 7. Yigong landslide simulation using different descriptions: (A) at 50 s using Eulerian method; (B) at 100 s using Eulerian method; (C) at 200 s using Eulerian method; (D) at 50 s using depth-averaged SPH; (E) at 100 s using depth-averaged SPH; (F) at 200 s using depth-averaged SPH.

Based on the above analysis, the Eulerian description is more suitable for flow-like motion, but the Lagrangian description is more suitable for the discrete rigid body motion. The description is one of the factors influencing the result.

4.2. Model Selection

Based on Varnes' classification [27], the materials include rock, debris (coarse soil), and earth (fine soil). Rock is a solid mass of geological materials, debris is scattered material (large rock fragments), and earth is a cohesive, plastic, clayey soil. These terms are neither geological nor geotechnical [32,34,35,73,74] but are related to the size, shape, quantity, and properties, which help us select a suitable description. A rock is a solid mass and an aggregate of minerals that can be considered a discontinuous rigid body in landslide dynamics due to its characteristics. "Earth" is neither a geological term nor a geotechnical term, and it describes construction material or agricultural soil [75]. Earth is defined

as a material in which at least 80% of particles are smaller than 2 mm [27]. Debris is a mixture of large and small blocks of rock, and debris motion involves multi-phase flow (20% to 80% of particles >2 mm). The properties of debris encompass the characteristics of both rigid bodies and fluids. Particle size is one of the critical factors to consider in the description of motion. When the material volume is small, and the quantity of material is large, the Eulerian description including the depth-averaged model is generally suitable for describing these motions. The Lagrangian description is suitable for large-volume and small-quantity discrete rigid body movement. The Eulerian–Lagrangian method may be suitable for the rock and soil aggregate movement.

In addition, the motion types include falling, sliding, spreading, and flowing. In falling and toppling, collisions and shearing are the major contact processes, and shearing is the main contact process in sliding, flowing, and spreading. This indicates that the movement type determines the force model in a given situation. Collision and friction are critical forces to change the movement state for falling and toppling. However, dry friction and viscosity need to be considered in sliding, spreading, and flowing. Therefore, landslide classification can guide the selection of models of landslide dynamics (Table 4).

Table 4. Relationship between models and types.

Motion	Rock	Earth	Debris
Falling and toppling	Force: collision, friction Motion: Lagrangian	Force: collision, friction Motion: Eulerian	Force: collision, friction Motion: Eulerian/Lagrangian
Sliding, spreading, and flowing	Force: dry friction and viscosity Motion: Lagrangian or Eulerian	Force: dry friction and viscosity Motion: Eulerian	Force: dry friction and viscosity Motion: Eulerian/Lagrangian

During the movement, the movement forms transform into each other. Fragmentation is a key process in rock movement and influences the whole process. Fragmentation can cause changes in movement form from falling to flowing [76]. As the number of debris increases due to fragmentation, the interactions in the debris become increasingly complex. From an energy perspective, fragmentation can result in energy dissipation [62] and drag reduction during fragmentation. After fragmentation, small debris has a lubricating effect, and large debris can be transported for a long distance. Therefore, fragmentation in long-runout landslides is very complicated [77]. The movement process gradually transforms from falling and bouncing to sliding and flowing. Therefore, a single-phase model is not suitable for these processes. We should build an episode-based multi-phase model on GIS platforms to describe different states. The best method is a rigid body model in the initial stage and a flow-like model after fragmentation. Therefore, we may use various model forms to obtain more accurate results in landslide simulation.

5. Conclusions

Based on the above analysis, we can draw the following conclusions:

- (1) A suitable model with proper assumptions can reduce uncertainties and simplify calculations. We must select suitable models to simulate different types of landslides. The proposed classification can provide some guidance for model selection. Landslide classification helps us understand landslide phenomena and select suitable dynamic models.
- (2) Compared with the two different models, the 3-D model can describe more details of the moving process than the depth-averaged model. Landslide runout zone, height, and speed are critical parameters in engineering design. The depth-averaged model meets the actual needs and provides engineering parameters quickly. Therefore, we can use the depth-averaged model to obtain the runout zones. If we pay more attention to the details, such as surge waves, the 3-D landslide simulation model is better.

- (3) A small difference in algorithms can produce a large difference in the runout zones. We should use as many algorithms as possible to obtain the trajectory for engineering design.
- (4) The number of elements, property, and material size determine the model selection. For discrete rigid body motion, models based on the Lagrangian description are suitable; for flow-like motion, models based on the Eulerian description are proper; for materials with various properties, models based on the Eulerian–Lagrangian description are best.

Author Contributions: Conceptualization, H.L. and Y.W.; methodology, Y.W.; software, Y.W. and A.T.; validation, H.L. and Y.W.; formal analysis, Y.W.; writing—original draft preparation, Y.W.; writing—review and editing, Y.W.; visualization, Y.W.; supervision, Y.W.; funding acquisition, H.L. and Y.W. All authors have read and agreed to the published version of the manuscript.

Funding: This research was supported by the Strategic Priority Research Program of the Chinese Academy of Sciences (CAS) (Grant No. XDA23090301), National Natural Science Foundation of China (Grant No. 41941019, 42041006), and the Second Tibetan Plateau Scientific Expedition and Research (STEP) program (Grant No. 2019QZKK0904).

Institutional Review Board Statement: Not applicable.

Informed Consent Statement: Not applicable.

Conflicts of Interest: The authors declare no conflict of interest.

References

1. McDougall, S. 2014 Canadian Geotechnical Colloquium: Landslide runout analysis—Current practice and challenges. *Can. Geotech. J.* **2017**, *54*, 605–620. [[CrossRef](#)]
2. Lo, C.-M.; Feng, Z.-Y.; Chang, K.-T. Landslide hazard zoning based on numerical simulation and hazard assessment. *Geomat. Nat. Hazards Risk* **2018**, *9*, 368–388. [[CrossRef](#)]
3. Pastor, M.; Blanc, T.; Haddad, B.; Petrone, S.; Sanchez Morles, M.; Dremptic, V.; Issler, D.; Crosta, G.; Cascini, L.; Sorbino, G. Application of a SPH depth-integrated model to landslide run-out analysis. *Landslides* **2014**, *11*, 793–812. [[CrossRef](#)]
4. Pedrazzini, A.; Froese, C.R.; Jaboyedoff, M.; Hungr, O.; Humair, F. Combining digital elevation model analysis and run-out modeling to characterize hazard posed by a potentially unstable rock slope at Turtle Mountain, Alberta, Canada. *Eng. Geol.* **2012**, *128*, 76–94. [[CrossRef](#)]
5. Sun, D.; Xu, J.; Wen, H.; Wang, D. Assessment of landslide susceptibility mapping based on Bayesian hyperparameter optimization: A comparison between logistic regression and random forest. *Eng. Geol.* **2021**, *281*, 105972. [[CrossRef](#)]
6. Liu, J.; Wu, Y.; Gao, X.; Zhang, X. A Simple Method of Mapping Landslides Runout Zones Considering Kinematic Uncertainties. *Remote Sens.* **2022**, *14*, 668. [[CrossRef](#)]
7. Fell, R.; Corominas, J.; Bonnard, C.; Cascini, L.; Leroi, E.; Savage, W.Z. Guidelines for landslide susceptibility, hazard and risk zoning for land-use planning. *Eng. Geol.* **2008**, *102*, 99–111. [[CrossRef](#)]
8. Glade, T.; Crozier, M.J. The nature of landslide hazard impact. In *Landslide Hazard Risk*; Wiley: Chichester, UK, 2005; pp. 43–74.
9. Lan, H.; Martin, C.D.; Lim, C.H. RockFall analyst: A GIS extension for three-dimensional and spatially distributed rockfall hazard modeling. *Comput. Geosci.* **2007**, *33*, 262–279. [[CrossRef](#)]
10. Stevens, W.D. RocFall, a Tool for Probabilistic Analysis, Design of Remedial Measures and Prediction of Rockfalls. Ph.D. Thesis, University of Toronto, Toronto, ON, Canada, 1998.
11. Dorren, L.K. Rockyfor3D (v5. 2) revealed—Transparent description of the complete 3D rockfall model. *ecorisQ Pap.* **2015**, *32*, 1–33.
12. Ouyang, C.; He, S.; Xu, Q.; Luo, Y.; Zhang, W. A MacCormack-TVD finite difference method to simulate the mass flow in mountainous terrain with variable computational domain. *Comput. Geosci.* **2013**, *52*, 1–10. [[CrossRef](#)]
13. FLO-2D. *FLO-2D Reference Manual*; FLO-2D Software Inc.: Nutrioso, AZ, USA, 2017.
14. Mergili, M.; Fischer, J.-T.; Krenn, J.; Pudasaini, S.P. Ravaflow v1, an advanced open-source computational framework for the propagation and interaction of two-phase mass flows. *Geosci. Model Dev.* **2017**, *10*, 553–569. [[CrossRef](#)]
15. Sheridan, M.F.; Stinton, A.J.; Patra, A.; Pitman, E.; Bauer, A.; Nichita, C. Evaluating Titan2D mass-flow model using the 1963 Little Tahoma peak avalanches, Mount Rainier, Washington. *J. Volcanol. Geotherm. Res.* **2005**, *139*, 89–102. [[CrossRef](#)]
16. Scaringi, G.; Fan, X.; Xu, Q.; Liu, C.; Ouyang, C.; Domènech, G.; Yang, F.; Dai, L. Some considerations on the use of numerical methods to simulate past landslides and possible new failures: The case of the recent Xinmo landslide (Sichuan, China). *Landslides* **2018**, *15*, 1359–1375. [[CrossRef](#)]
17. Chang, Y.-S.; Chang, T.-J. SPH simulations of solute transport in flows with steep velocity and concentration gradients. *Water* **2017**, *9*, 132. [[CrossRef](#)]
18. Mishra, B.; Rajamani, R.K. The discrete element method for the simulation of ball mills. *Appl. Math. Model.* **1992**, *16*, 598–604. [[CrossRef](#)]

19. Rigaux, P.; Scholl, M.; Voisard, A. *Spatial Databases: With Application to GIS*; Morgan Kaufmann: Burlington, MA, USA, 2002.
20. Heim, A. *Landslides and Human Lives (Bergsturz und Menschenleben)*; Bi-Tech Publishers: Vancouver, BC, USA, 1932; p. 196.
21. Zaruba, Q.; Mencl, V. *Landslides and Their Control*; Elsevier: Amsterdam, The Netherlands, 2014.
22. Sharpe, C. *Landslides and Related Phenomena*; Columbia University Press: New York, NY, USA, 1938.
23. Hungr, O.; Leroueil, S.; Picarelli, L. The Varnes classification of landslide types, an update. *Landslides* **2014**, *11*, 167–194. [[CrossRef](#)]
24. Varnes, D.J. Landslide types and processes. *Landslides Eng. Pract.* **1958**, *24*, 20–47.
25. Cruden, D.; Varnes, D. Landslide types and processes. In *Landslides-Investigation and Mitigation*; National Research Council Transportation Research Board Special Report 247; Turner, K.A., Schuster, R.L., Eds.; Transportation Research Board: Washington, DC, USA, 1996.
26. WP/WLI. *UNESCO Working Party for World Landslide Inventory G 1993*; BiTech Publishers Ltd.: Richmond, BC, Canada, 1993.
27. Varnes, D.J. Slope movement types and processes. *Spec. Rep.* **1978**, *176*, 11–33.
28. Dorren, L.K. A review of rockfall mechanics and modelling approaches. *Prog. Phys. Geogr.* **2003**, *27*, 69–87. [[CrossRef](#)]
29. Iverson, R.M. Landslide triggering by rain infiltration. *Water Resour. Res.* **2000**, *36*, 1897–1910. [[CrossRef](#)]
30. Wang, Y.; Xu, G. Back-Analysis of Water Waves Generated by the Xintan Landslide. In *Landslide Disaster Mitigation in Three Gorges Reservoir, China*; Springer: Berlin/Heidelberg, Germany, 2009; pp. 433–445.
31. Wu, Y.; Lan, H. Debris flow analyst (DA): A debris flow model considering kinematic uncertainties and using a GIS platform. *Eng. Geol.* **2020**, *279*, 105877. [[CrossRef](#)]
32. Iverson, R.M.; Denlinger, R.P. Flow of variably fluidized granular masses across three-dimensional terrain: 1. Coulomb mixture theory. *J. Geophys. Res. Solid Earth* **2001**, *106*, 537–552. [[CrossRef](#)]
33. Iverson, R.M. The physics of debris flows. *Rev. Geophys.* **1997**, *35*, 245–296. [[CrossRef](#)]
34. Savage, S.B.; Hutter, K. The motion of a finite mass of granular material down a rough incline. *J. Fluid Mech.* **1989**, *199*, 177–215. [[CrossRef](#)]
35. Pudasaini, S.P. A general two-phase debris flow model. *J. Geophys. Res. Earth Surf.* **2012**, *117*, 1–28. [[CrossRef](#)]
36. Denlinger, R.P.; Iverson, R.M. Granular avalanches across irregular three-dimensional terrain: 1. Theory and computation. *J. Geophys. Res. Earth Surf.* **2004**, *109*, 1–16. [[CrossRef](#)]
37. Pudasaini, S.P.; Mergili, M. A multi-phase mass flow model. *J. Geophys. Res. Earth Surf.* **2019**, *124*, 2920–2942. [[CrossRef](#)]
38. Pudasaini, S.P.; Krautblatter, M. The mechanics of landslide mobility with erosion. *Nat. Commun.* **2021**, *12*, 6793. [[CrossRef](#)]
39. Pudasaini, S.P.; Fischer, J.-T. A mechanical erosion model for two-phase mass flows. *Int. J. Multiph. Flow* **2020**, *132*, 103416. [[CrossRef](#)]
40. Worgull, M. Chapter 3—Molding Materials for Hot Embossing. In *Hot Embossing*; Worgull, M., Ed.; William Andrew Publishing: Boston, MA, USA, 2009; pp. 57–112.
41. Zeng, S.; Migórski, S. A class of time-fractional hemivariational inequalities with application to frictional contact problem. *Commun. Nonlinear Sci. Numer. Simul.* **2018**, *56*, 34–48. [[CrossRef](#)]
42. Evans, S.; Hungr, O. The assessment of rockfall hazard at the base of talus slopes. *Can. Geotech. J.* **1993**, *30*, 620–636. [[CrossRef](#)]
43. Pfeiffer, T.J. *Rockfall Hazard Analysis Using Computer Simulation of Rockfalls*. Ph.D. Thesis, Colorado School of Mines, Golden, CO, USA, 1989.
44. Spadari, M.; Kardani, M.; De Carteret, R.; Giacomini, A.; Buzzi, O.; Fityus, S.; Sloan, S. Statistical evaluation of rockfall energy ranges for different geological settings of New South Wales, Australia. *Eng. Geol.* **2013**, *158*, 57–65. [[CrossRef](#)]
45. Guzzetti, F.; Crosta, G.; Detti, R.; Agliardi, F. STONE: A computer program for the three-dimensional simulation of rock-falls. *Comput. Geosci.* **2002**, *28*, 1079–1093. [[CrossRef](#)]
46. Li, L.; Lan, H. Probabilistic modeling of rockfall trajectories: A review. *Bull. Eng. Geol. Environ.* **2015**, *74*, 1163–1176. [[CrossRef](#)]
47. Tskhakaya, D.; Matyash, K.; Schneider, R.; Taccogna, F. The Particle-In-Cell Method. *Contrib. Plasma Phys.* **2007**, *47*, 563–594. [[CrossRef](#)]
48. Pastor, M.; Haddad, B.; Sorbino, G.; Cuomo, S.; Drempetic, V. A depth-integrated, coupled SPH model for flow-like landslides and related phenomena. *Int. J. Numer. Anal. Methods Geomech.* **2009**, *33*, 143–172. [[CrossRef](#)]
49. Lin, C.; Pastor, M.; Li, T.; Liu, X.; Qi, H.; Lin, C. A SPH two-layer depth-integrated model for landslide-generated waves in reservoirs: Application to Halaowo in Jinsha River (China). *Landslides* **2019**, *16*, 2167–2185. [[CrossRef](#)]
50. Longo, A.; Pastor, M.; Sanavia, L.; Manzanal, D.; Martin Stickle, M.; Lin, C.; Yague, A.; Tayyebi, S.M. A depth average SPH model including μ (I) rheology and crushing for rock avalanches. *Int. J. Numer. Anal. Methods Geomech.* **2019**, *43*, 833–857. [[CrossRef](#)]
51. Agliardi, F.; Crosta, G.B. High resolution three-dimensional numerical modelling of rockfalls. *Int. J. Rock Mech. Min. Sci.* **2003**, *40*, 455–471. [[CrossRef](#)]
52. Woltjer, M.; Rammer, W.; Brauner, M.; Seidl, R.; Mohren, G.; Lexer, M. Coupling a 3D patch model and a rockfall module to assess rockfall protection in mountain forests. *J. Environ. Manag.* **2008**, *87*, 373–388. [[CrossRef](#)]
53. Bartelt, P.; Bieler, C.; Bühler, Y.; Christen, M.; Christen, M.; Dreier, L.; Gerber, W.; Glover, J.; Schneider, M.; Glocker, C. *RAMMS: Rockfall User Manual v1. 6*; WSL Institute for Snow and Avalanche Research SLF: Davos, Switzerland, 2016.
54. Matas, G.; Lantada, N.; Corominas, J.; Gili, J.; Ruiz-Carulla, R.; Prades, A. RockGIS: A GIS-based model for the analysis of fragmentation in rockfalls. *Landslides* **2017**, *14*, 1565–1578. [[CrossRef](#)]
55. Christen, M.; Kowalski, J.; Bartelt, P. RAMMS: Numerical simulation of dense snow avalanches in three-dimensional terrain. *Cold Reg. Sci. Technol.* **2010**, *63*, 1–14. [[CrossRef](#)]

56. Molinari, M.E.; Cannata, M.; Begueria, S.; Ambrosi, C. GIS-based Calibration of MassMov2D. *Trans. GIS* **2012**, *16*, 215–231. [[CrossRef](#)]
57. Wu, Y.; Lan, H. Landslide Analyst—A landslide propagation model considering block size heterogeneity. *Landslides* **2019**, *16*, 1107–1120. [[CrossRef](#)]
58. de’Michieli Vitturi, M.; Esposti Ongaro, T.; Lari, G.; Aravena, A. IMEX_SfloW2D 1.0: A depth-averaged numerical flow model for pyroclastic avalanches. *Geosci. Model Dev.* **2019**, *12*, 581–595. [[CrossRef](#)]
59. Berger, M.J.; George, D.L.; LeVeque, R.J.; Mandli, K.T. The GeoClaw software for depth-averaged flows with adaptive refinement. *Adv. Water Resour.* **2011**, *34*, 1195–1206. [[CrossRef](#)]
60. Hungr, O.; McDougall, S. Two numerical models for landslide dynamic analysis. *Comput. Geosci.* **2009**, *35*, 978–992. [[CrossRef](#)]
61. Amicarelli, A.; Manenti, S.; Albano, R.; Agate, G.; Paggi, M.; Longoni, L.; Mirauda, D.; Ziane, L.; Viccione, G.; Todeschini, S. SPHERA v. 9.0. 0: A Computational Fluid Dynamics research code, based on the Smoothed Particle Hydrodynamics mesh-less method. *Comput. Phys. Commun.* **2020**, *250*, 107157. [[CrossRef](#)]
62. Li, X.; Tang, X.; Zhao, S.; Yan, Q.; Wu, Y. MPM evaluation of the dynamic runout process of the giant Daguangbao landslide. *Landslides* **2021**, *18*, 1509–1518. [[CrossRef](#)]
63. Crosta, G.; Imposimato, S.; Roddeman, D. Numerical modelling of entrainment/deposition in rock and debris-avalanches. *Eng. Geol.* **2009**, *109*, 135–145. [[CrossRef](#)]
64. Jasak, H.; Jemcov, A.; Tukovic, Z. OpenFOAM: A C++ library for complex physics simulations. In Proceedings of the International Workshop on Coupled Methods in Numerical Dynamics, Dubrovnik, Croatia, 19–21 September 2007; pp. 1–20.
65. Ramachandran, P. PySPH: A reproducible and high-performance framework for smoothed particle hydrodynamics. In Proceedings of the 15th Python in Science Conference, Austin, TX, USA, 11–17 July 2016; pp. 127–135.
66. Wang, J.-S.; Ni, H.-G.; He, Y.-S. Finite-difference TVD scheme for computation of dam-break problems. *J. Hydraul. Eng.* **2000**, *126*, 253–262. [[CrossRef](#)]
67. Ming, H.T.; Chu, C.R. Two-dimensional shallow water flows simulation using TVD-MacCormack scheme. *J. Hydraul. Res.* **2000**, *38*, 123–131. [[CrossRef](#)]
68. Delaney, K.B.; Evans, S.G. The 2000 Yigong landslide (Tibetan Plateau), rockslide-dammed lake and outburst flood: Review, remote sensing analysis, and process modelling. *Geomorphology* **2015**, *246*, 377–393. [[CrossRef](#)]
69. Guo, C.; Montgomery, D.R.; Zhang, Y.; Zhong, N.; Fan, C.; Wu, R.; Yang, Z.; Ding, Y.; Jin, J.; Yan, Y. Evidence for repeated failure of the giant Yigong landslide on the edge of the Tibetan Plateau. *Sci. Rep.* **2020**, *10*, 14371. [[CrossRef](#)]
70. Kang, C. Modelling Entrainment in Debris Flow Analysis for Dry Granular Material. *Int. J. Geomech.* **2016**, *17*, 04017087. [[CrossRef](#)]
71. Zhuang, Y.; Yin, Y.; Xing, A.; Jin, K. Combined numerical investigation of the Yigong rock slide-debris avalanche and subsequent dam-break flood propagation in Tibet, China. *Landslides* **2020**, *17*, 2217–2229. [[CrossRef](#)]
72. Voellmy, A. Die Zerstörungs-Kraft von lawinen, Sonderdruck aus der Schweiz. *Bauzeitung* **1955**, *73*, 159–165.
73. Morgenstern, N.R. The evaluation of slope stability—A 25 year perspective. In Proceedings of the Stability and Performance of Slopes and Embankments II, Berkeley, CA, USA, 29 June–1 July 1992; pp. 1–26.
74. Leroueil, S.; Locat, J.; Vaunat, J.; Picarelli, L.; Lee, H. Geotechnical characterization of slope movements. In Proceedings of the Landslides, Trondheim, Norway, 17–21 June 1996; pp. 53–74.
75. Bates, R.L.; Jackson, J.A. *Dictionary of Geological Terms*; Anchor Books: New York, NY, USA, 1984; Volume 584.
76. Ruiz-Carulla, R.; Corominas, J.; Mavrouli, O. A fractal fragmentation model for rockfalls. *Landslides* **2017**, *14*, 875–889. [[CrossRef](#)]
77. Davies, T.; McSaveney, M.; Hodgson, K. A fragmentation-spreading model for long-runout rock avalanches. *Can. Geotech. J.* **1999**, *36*, 1096–1110. [[CrossRef](#)]